Intracellular Self-Assembly and Disassembly of ^{19}F Nanoparticles Confer Respective "Off" and "On" ^{19}F NMR/MRI Signals for Legumain Activity Detection in Zebrafish

Yue Yuan,[†] Shuchao Ge,[‡] Hongbin Sun,[§] Xuejiao Dong,[†] Hongxin Zhao,[§] Linna An,[†] Jia Zhang,[†] Junfeng Wang,[§] Bing Hu,[‡] and Gaolin Liang*,[†]

[†]CAS Key Laboratory of Soft Matter Chemistry, Department of Chemistry and [‡]School of Life Sciences, University of Science and Technology of China, 96 Jinzhai Road, Hefei, Anhui 230026, China and [§]High Magnetic Field Laboratory, Hefei Institutes of Physical Science, Chinese Academy of Sciences, 350 Shushanhu Road, Hefei, Anhui 230031, China

ABSTRACT ^{19}F MRI has higher selectivity but lower sensitivity than ^{1}H MRI for *in vivo* diagnosis. Therefore, to avoid using a high injection dose of the ^{19}F probe while, in the meantime, maintaining the high sensitivity of ^{19}F MRI has remained challenging. Local self-assembly and disassembly of ^{19}F nanoparticles could be one of the "smart" strategies to achieve this goal. Herein, we report a dual-functional probe 1 for glutathione (GSH)-controlled self-assembly and subsequent legumain (Lgmn)-controlled disassembly of its nanoparticles (*i.e.*, 1-NPs). Self-assembly and disassembly of 1-NPs confer ^{19}F magnetic resonance (MR) signals "off" and "on", respectively. Employing this strategy, we successfully applied 1 for consecutive detections of GSH and Lgmn *in vitro* and in cells, imaging Lgmn activity in HEK 293T tumors in zebrafish at a low dosage under 14.1 T.

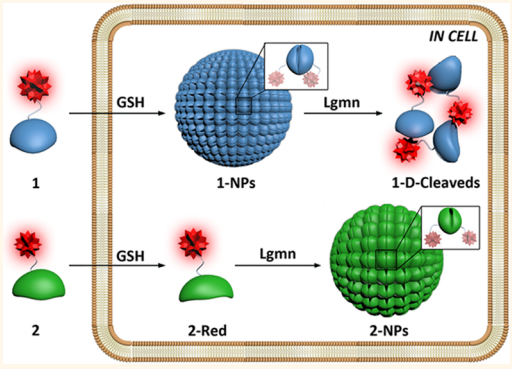

KEYWORDS: ^{19}F MRI · self-assembly · disassembly · legumain · zebrafish

Legumain (Lgmn) is an asparaginyl endopeptidase which belongs to the C13 family of cysteine proteases.[1] It has been found in the seeds of leguminous plants, in *Schistosoma mansoni*, and in mammalian tissues such as kidney and placenta, in which it associates with normal protein catabolism and renal homeostasis.[2,3] Lgmn can degrade fibronectin and therefore promote the remodeling of the extracellular matrix in proximal tubule cells.[4] Additionally, it plays important roles in the initial invariant chain processing of antigens for MHC class II presentation and in the inhibition of osteoclast formation and bone resorption.[5,6] Beyond its roles in normal physiology, Lgmn is also associated with several inflammatory diseases such as atherosclerosis, stroke, and cancer. It overexpresses in a majority of tumors (including carcinomas of the breast, colon, and prostate) and in central nervous system neoplasms.[4] Lgmn-overexpressed HEK 293 cells have been demonstrated to be very aggressive in migration, invasion, and angiogenesis.[7] Compared with nontransfected control cells, these Lgmn-overexpressed cells also show increased metastasis from subcutaneous tumors *in vivo*.[7] Although Lgmn is likely associated with most malignancies, precise roles for stromal-derived Lgmn have not been thoroughly defined.[8] This calls for more sensitive and biocompatible methods to assay Lgmn activity *in vitro* and *in vivo*. Since Lgmn has its unique peptide substrates with asparaginyl residues in the P1 position for hydrolysis,[1,2] it is advantageous for chemists to design peptide-based probes for the specific detection of Lgmn.

* Address correspondence to gliang@ustc.edu.cn.

Received for review January 14, 2015 and accepted April 13, 2015.

Published online April 13, 2015
10.1021/acsnano.5b00287

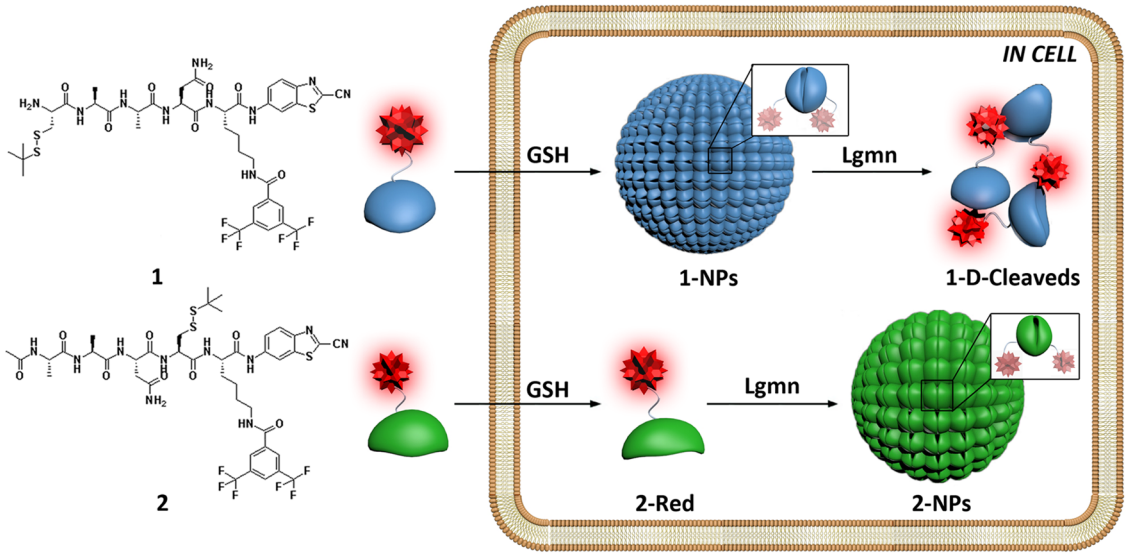

Figure 1. Schematic illustration of intracellular GSH-controlled self-assembly followed by Lgmn-controlled disassembly of 1-NPs, showing respective "off" and "on" ^{19}F NMR signals for Lgmn detection, and Lgmn-controlled self-assembly of 2-NPs results in ^{19}F NMR signals "off" inside cells.

Magnetic resonance imaging (MRI) is one of the noninvasive, powerful techniques for *in vivo* and *ex vivo* visualization of biomarkers and species. It provides us with abundant information on the delicate structures deeply inside vital organisms.[9−13] Up to date, ^{1}H MRI has been widely used for both clinical and experimental diagnoses due to its high sensitivity contributed to the abundance of water in the vicinity of contrast agents. However, ^{1}H MRI suffers from low contrast-to-noise ratio due to the large background signals from the protons of bulk water. In our bodies, ^{19}F atoms are concentrated in salts of solid form mostly in bones and teeth.[14] Thus, the transverse relaxation time (T_2) of the intrinsic ^{19}F is extremely shortened,[15] and its MRI signal is hardly detectable. When a ^{19}F compound is administered to a patient, only the extrinsic ^{19}F MRI signals can be monitored without interference from background signals. Therefore, ^{19}F MRI possesses better contrast-to-noise ratio than ^{1}H MRI but with a comparable sensitivity (83% relative to ^{1}H). Due to their close γ (gyromagnetic ratio) values, ^{19}F NMR can be recorded on most ^{1}H NMR instruments by appropriately tuning the RF coils.[14,16] For these above reasons, functional probes for ^{19}F NMR/MRI are very attractive to chemical biology, medicine, pharmaceuticals, and molecular imaging. To date, a variety of fluorinated compounds have been developed for ^{19}F NMR/MRI to assess biomarkers and biological events such as gene transfection,[17] protein monitoring,[18−20] enzymatic activity,[14,21,22] and environmental alteration.[23−25] Nevertheless, it is also always necessary to inject large doses of ^{19}F probes to generate enough contrast-to-noise ratio in the region-of-interest (ROI) for detection. This calls for a "smart" strategy which can locally release a large amount of ^{19}F probes in the ROI and also decrease the injection dose of the probe.

Since ^{19}F has a relatively large chemical shift anisotropy (approximately 39 ppm for a $-CF_3$ group), the transverse relaxation of its signals in ^{19}F NMR spectroscopy is extremely sensitive to the apparent molecular mass. Therefore, formation of a large molecular assembly causes severe broadening of the ^{19}F MR signal in the ^{19}F NMR spectroscopy, but disassembly recovers it.[18,20,26] Inspired by these above-mentioned details, as shown in Figure 1, in this work, we developed a "smart" ^{19}F probe Cys(StBu)-Ala-Ala-Asn-Lys(FMBA)-CBT (**1**) which first self-assembles into its nanoparticles (*i.e.*, **1-NPs**) upon glutathione (GSH) reduction inside cells and then the nanoparticles are disassembled by Lgmn, ultimately turning the ^{19}F NMR/MRI signal "on" for Lgmn detection. A control compound Ac-Ala-Ala-Asn-Cys(StBu)-Lys(FMBA)-CBT (**2**), whose ^{19}F NMR/MRI signal was designed to be turned "off" inside cells, was synthesized and studied in parallel (Figure 1).

RESULTS AND DISCUSSION

Rationale of the Design. The rationale of our design is shown in Figure 1. Based on a biocompatible condensation reaction recently developed by Rao and coworkers,[27,28] **1** was designed to have these components: (1) a disulfided cysteine (Cys) motif, after being reduced by intracellular GSH to expose the reactive 1,2-aminothiol group, condenses with the cyano group of the 2-cyanobenzothiazole (CBT) motif to yield macrocyclized oligomers which self-assemble into nanoparticles (*i.e.*, **1-NPs**), turning "off" the ^{19}F NMR signals; (2) an alanine−alanine−asparagine (AAN) substrate for Lgmn cleavage to disassemble **1-NPs** and turn "on" the ^{19}F NMR signals; and (3) a FMBA motif conjugating to the side chain of a lysine (Lys) motif to introduce ^{19}F NMR signal source. The control compound **2**, whose NH_2 group of disulfided Cys motif is caged by AAN, is

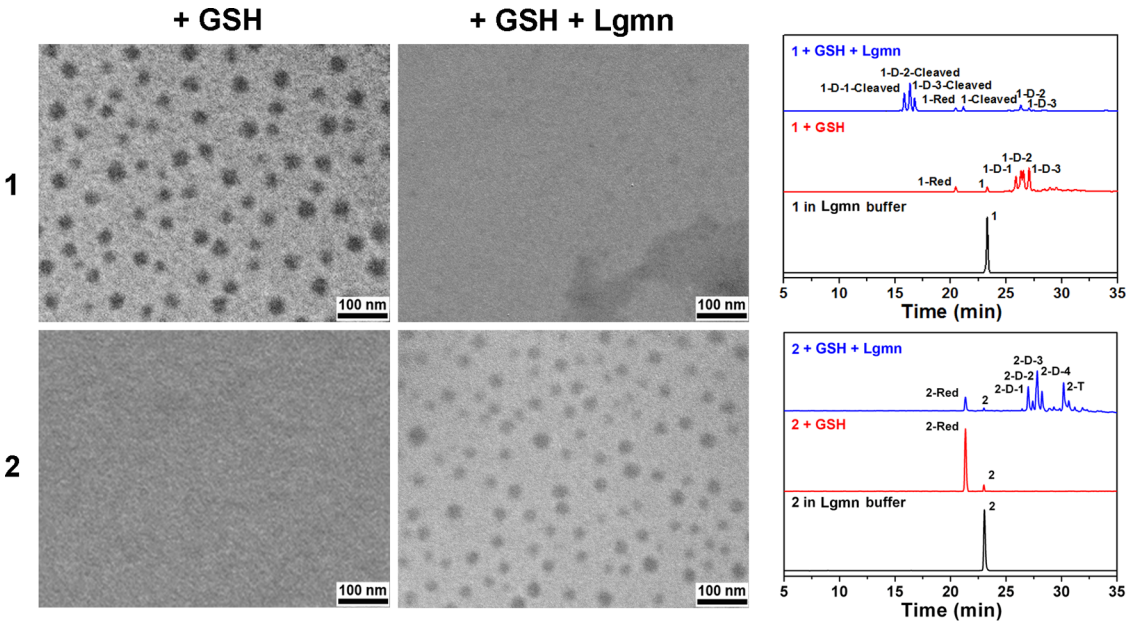

Figure 2. Left: TEM images of 1-NPs (top, 500 μM 1 treated with 2.5 mM GSH for 30 min) and GSH-treated 2 (bottom, 500 μM 2 treated with 2.5 mM GSH for 30 min). Middle: TEM images of 1-NPs after being incubated with 25 nmol/μg Lgmn at 37 °C for 14 h (top) and 2-NPs (bottom, 500 μM 2 treated with 2.5 mM GSH for 30 min first then incubated with 25 nmol/μg Lgmn at 37 °C for 14 h). Top right: HPLC traces of 500 μM 1 in Lgmn working buffer (black), 500 μM 1 treated with 2.5 mM GSH for 30 min (red), and 500 μM 1 first treated with 2.5 mM GSH for 30 min and then incubated with 25 nmol/μg Lgmn at 37 °C for 14 h (blue). Bottom right: HPLC traces of 500 μM 2 in Lgmn working buffer (black), 500 μM 2 treated with 2.5 mM GSH for 30 min (red), and 500 μM 2 first treated with 2.5 mM GSH for 30 min and then incubated with 25 nmol/μg Lgmn at 37 °C for 14 h (blue).

first subjected to GSH reduction of the disulfide bond to yield **2-Red** inside cells, leaving the ^{19}F NMR signals "on". Subsequent Lgmn cleavage of the AAN substrate of **2-Red** initiates the condensation reaction and self-assembly of the nanoparticles (*i.e.*, **2-NPs**), turning the ^{19}F NMR signals "off". The syntheses and characterizations of **1** and **2** are described in the Supporting Information (Figures S1−S4).

GSH-Controlled Self-Assembly and Lgmn-Controlled Disassembly of 1-NPs. After the syntheses of **1** and **2**, we validated the GSH-controlled self-assembly and Lgmn-controlled disassembly of **1-NPs** and the Lgmn-controlled self-assembly of **2-NPs**. For **1** at 500 μM, after the addition of 2.5 mM GSH and incubation at 37 °C for 30 min, the disulfide bond of **1** was reduced by GSH, exposing the 1,2-aminothiol group which instantly condenses with the CBT moiety of another monomer to form cyclized oligomers (most of them are dimers, **1-Ds**). Subsequently, these amphiphilic oligomers self-assemble into monodispersive nanoparticles (**1-NPs**) *via* the $\pi-\pi$ stackings among each other. Formation of **1-NPs** was confirmed by the obvious increases of the absorptions of **1** at 500−700 nm on the UV−vis spectra (Figure S5a). After that, we incubated the monodispersions with 25 nmol/μg Lgmn in buffer at 37 °C for 14 h to disassemble **1-NPs**. The NPs in the two dispersions (*i.e.*, before and after Lgmn addition) were analyzed with transmission electron microscope (TEM) (Figure 2). For **2** at 500 μM, after the addition of 2.5 mM GSH and incubation at 37 °C for 30 min, its disulfide bond was reduced by GSH to yield the reduction product **2-Red**, which is more hydrophilic than **2** and could not self-assemble into NPs. Subsequent incubation of 25 nmol/μg Lgmn with **2-Red** resulted in the cleavage of the AAN substrate, exposing the 1,2-aminothiol group, which condenses with the cyano group on the CBT moiety of another monomer to form macrocyclized amphiphilic oligomers (most of them are dimers, **2-Ds**). Similarly, these amphiphilic oligomers self-assembled into monodispersive nanoparticles (**2-NPs**) *via* the $\pi-\pi$ stackings among each other. Formation of **2-NPs** was also identified by the change of the absorptions at 500−700 nm on the UV−vis spectra (Figure S5b) and TEM (Figure 2). As shown in Figure 2, TEM images showed that the fluorinated NPs of **1** (*i.e.*, **1-NPs**) and **2** (*i.e.*, **2-NPs**) have average diameters of 25 $\pm$ 7 and 21 $\pm$ 6 nm, respectively (left and middle columns of Figure 2). The statistical results of diameters of NPs in the TEM images are shown in Figure S6. Dynamic light scattering (DLS) measurements of the dispersions indicated that **1-NPs** have a mean hydrated diameter of 62 nm, while Lgmn-treated **1-NPs** have a mean hydrated diameter of 9 nm (Figure S7a), echoing that **1-NPs** were cleaved by Lgmn and disassembled, and the **2-NPs** have a mean hydrated diameter of about 55 nm (Figure S7b).

To chemically validate the GSH-controlled condensation and subsequent Lgmn-controlled cleavage of **1**, we directly injected the above incubation mixtures into a high-performance liquid chromatography (HPLC)

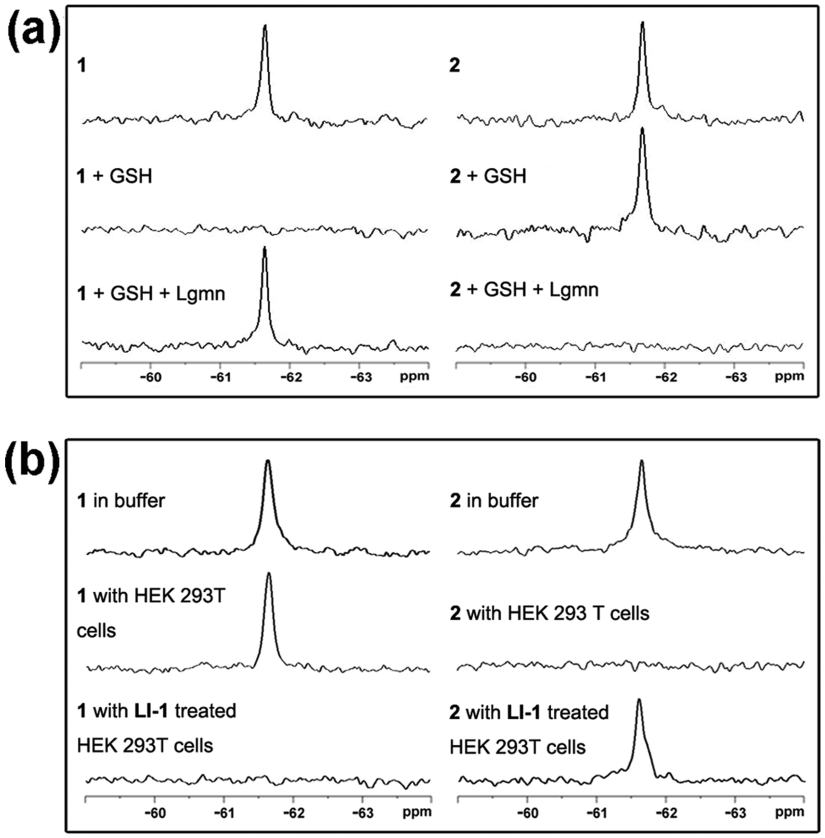

Figure 3. (a) ^{19}F NMR spectra of 1 or 2 at 500 μM in water (top), in the presence of 2.5 mM GSH for 30 min (middle), and in the presence of 2.5 mM GSH for 30 min followed by incubation with 25 nmol/μg Lgmn at 37 °C for 14 h (bottom). (b) ^{19}F NMR spectra of 1 or 2 at 500 μM in 100 μL of RIPA lysis buffer (top), in cell lysate after being incubated with HEK 293T cells at 37 °C for 1 h (middle), and in cell lysate after being incubated at 37 °C for 1 h with HEK 293T cells pretreated with 100 μM LI-1 for 1 h (bottom).

system and collected the peaks for matrix-assisted laser desorption/ionization (MALDI) mass spectroscopic analysis. After 500 μM **1** was treated with 2.5 mM GSH, as shown in the top right panel of Figure 2, we identified a new peak at retention time of 20.5 min that appeared on the HPLC trace as the reduction product of **1** (*i.e.*, **1-Red**, Figure S8). The peaks on the HPLC trace at retention times of 25.9, 26.5, and 27.1 min were identified as the isomeric condensation products of **1** (*i.e.*, dimers, **1-Ds**, Figure S9). Further addition of 25 nmol/μg Lgmn to the reaction mixture and incubation at 37 °C for another 14 h resulted in three new HPLC peaks at retention times of 15.8, 16.3, and 16.7 min, which were identified as the corresponding cleaved products of **1-Ds** by Lgmn (*i.e.*, **1-D-Cleaved**s, Figure S10), suggesting that the condensation products of **1** (*i.e.*, **1-Ds**) are cleavable by Lgmn. The tiny HPLC peak at retention time of 21.1 min, which accounted for 2.3% of the total products, was identified as the directly cleaved product of **1** by Lgmn (*i.e.*, **1-Cleaved**, Figure S11). For comparison, as shown in the bottom right panel of Figure 2, treatment of 500 μM **2** with 2.5 mM GSH only yielded the reduction product of **2** (*i.e.*, **2-Red**, Figure S12), which has a retention time of 21.3 min on the HPLC trace. After further addition of Lgmn, new products which have HPLC retention times of 27.0, 27.4, 27.8, and 28.2 min were identified as the dimeric condensation isomers of **2-Red** (*i.e.*, dimers, **2-Ds**, Figure S13), and the new peak at retention time of 30.2 min was identified as the trimeric condensation product of **2-Red** (*i.e.*, **2-T**, Figure S14).

"Off" and "On" ^{19}F NMR Spectra of 1 for Respective Detection of GSH and Lgmn *in Vitro* and in Cells. Corresponding ^{19}F NMR spectra of **1**, **1** treated with GSH (*i.e.*, formation of **1-NPs**), and **1** treated with GSH followed by addition of Lgmn (*i.e.*, cleavage and disassembly of **1-NPs**) are shown in the left column of Figure 3a. Clearly, we observed the disappearance of the ^{19}F NMR signal of **1** at −61.7 ppm after it was treated with GSH for 30 min, suggesting that the formation of **1-NPs** induces fast transverse relaxation of the ^{19}F NMR signal. After the **1-NPs** were incubated with Lgmn for 14 h, the ^{19}F NMR signal at −61.7 ppm was recovered due to the hydrolysis and disassembly of **1-NPs** by Lgmn. Relaxation time measurement showed that the transverse relaxation times (T_2) of the ^{19}F magnetic spins in the above three solutions were 501 ± 6 ms, not detectable (ND), and 486 ± 23 ms, respectively (Table S1). In comparison, as shown in the right column of Figure 3a, treatment of **2** with GSH did not induce obvious change of the ^{19}F NMR signal at −61.7 ppm. However, further incubation of the mixture with Lgmn resulted in the

disappearance of ^{19}F NMR signal due to the formation of **2-NPs**, and T_2 relaxation times of the above three solutions were measured to be 483 ± 8 ms, 469 ± 10 ms, and ND, respectively (Table S2). Interestingly, when we incubated **1** in the presence of a mixture of 2.5 mM GSH and 25 nmol/μg Lgmn and studied their ^{19}F NMR spectra over time, we found that the ^{19}F NMR signal of **1** at −61.7 ppm first disappeared at 30 min, started to reappear at 2 h, and was almost restored at 12 h (Figure S15). TEM images of **1** in the presence of the mixture of 2.5 mM GSH and 25 nmol/μg Lgmn clearly showed the appearance of **1-NPs** at 30 min and the disappearance of the NPs at 12 h (Figure S16). These results indicated that GSH-controlled assembly and subsequent Lgmn-controlled disassembly of **1-NPs** confer ^{19}F NMR signals of **1** "off" and then "on", which in turn could be applied for the consecutive detections of GSH and Lgmn, respectively. The processes of the "off−on" ^{19}F NMR signals of **1** could be monitored stepwise by changing the concentrations of GSH and Lgmn added (Figure S17). The temporal dynamics of the Lgmn-induced "turn-on" procedure was also tracked, as shown in Figure S18.

After that, we also applied **1** to detect GSH and Lgmn in HEK 293T cells. HEK 293T is one of the cell lines that overexpress Lgmn, indicated by our Western blotting results, as shown in Figure S19. Following the synthetic method reported,[29] we also synthesized a legumain-specific inhibitor **LI-1** (Figure S20) for the following study. The untreated HEK 293T cell lysate, which does not have any detectable ^{19}F NMR signal (Figure S21), was used as the control. In principle, after being internalized by HEK 293T cells, **1** sequentially undergoes GSH-controlled self-assembly and subsequent Lgmn-controlled disassembly of **1-NPs**. Therefore, the ^{19}F NMR signal of **1** in HEK 293T cells should ultimately be "on", as shown in the left column of Figure 3b. To ensure that the "on" signal is induced by the Lgmn-controlled disassembly of **1-NPs**, we preincubated the cells with **LI-1** for 1 h before incubating them with **1**. Clearly, we observed that the ^{19}F NMR signal from the cells was "off" (Figure 3b) because **1** was only subjected to GSH-controlled reduction for the self-assembly of **1-NPs**. To further verify that the "on" signal was induced by intracellular Lgmn located in membrane organelles (*e.g.*, mitochondria, lysosomes, peroxisomes, *etc.*),[7,30] we fractionated HEK 293T cells after their incubation with **1**.[31,32] The results indicated that the cell pellet sample P (plasma membrane, microsomal fraction, and large polyribosomes) had the strongest ^{19}F NMR signal, whereas the pellet sample M (mitochondria, lysosomes, and peroxisomes) had a relatively weaker but obvious ^{19}F NMR signal (Figure S22). ^{19}F NMR signals from samples N (nuclei), R (ribosomal subunits, small polyribosomes), and C (cytosol) were barely detectable (Figure S22). With the ^{19}F NMR integral calibration curve of **1** in Figure S23, we could calculate that, after 1 h incubation with HEK 293 cells at 500 μM and 37 °C, about 13.75 fmol/cell of **1** was taken up by the cells. Specifically, about 6.98 and 5.72 fmol/cell of uptaken **1** was located in organelles M and P, respectively. In addition to **1**, we also applied **2** for the cell study. As shown in the right column of Figure 3b, HEK 293T cells incubated with **2** did not show an obvious ^{19}F NMR signal because **2** in the cells was finally subjected to the Lgmn-controlled condensation for the self-assembly of **2-NPs**. When the cells were pretreated with **LI-1** and then incubated with **2**, the ^{19}F NMR signal remained "on" because **2** was only subjected to GSH reduction and there was no nanoparticle formed in the cells (Figure 3b). HPLC analyses were performed to characterize the GSH-controlled self-assembly and Lgmn-controlled disassembly of **1-NPs**, as well as the GSH-controlled reduction of **2** and Lgmn-controlled self-assembly of **2-NPs** in HEK 293T cells throughout the experiments (Figure S24). We observed that the main products of **1** incubated with HEK 293T cells were Lgmn-cleaved dimers of **1** (*i.e.*, **1-D-Cleaveds** at 15.8, 16.3, and 16.7 min on the green HPLC trace of Figure S24a). Only a small portion of **1** was directly cleaved by Lgmn (i.e., **1-Cleaved** at 21.1 min on the green HPLC trace of Figure S24a). The peak area ratio of **1-D-Cleaveds** over **1-Cleaved** is about 12:1. Interestingly, only GSH-controlled oligomeric products of **1** (*i.e.*, dimers, **1-Ds** at 25.9, 26.5, and 27.1 min on the purple HPLC trace of Figure S24a) were observed in **LI-1**-treated HEK 293T cells, suggesting the above **1-D-Cleaveds** are actually resulted from Lgmn cleavage of **1-Ds**. Products of **2** in HEK 293T cells were only Lgmn-controlled oligomeric condensation products of **2** (*i.e.*, dimers, **2-Ds** at 27.0, 27.4, 27.8, and 28.2 min and trimer **2-T** at 30.2 min on the green HPLC trace of Figure S24b). When **2** was incubated with **LI-1**-treated HEK 293T cells, only the GSH-controlled reduction product of **2** (*i.e.*, **2-Red** at 21.3 min on the purple HPLC trace of Figure S24b) could be detected, suggesting that the above-mentioned **2-Ds** actually resulted from Lgmn-cleavage-controlled condensation of **2**. The retention times of these HPLC peaks agreed well with those peaks on the blue or red HPLC traces in Figure 2, which were characterized with MALDI-MS. From the HPLC trace in Figure S24a (green trace) and the calibration curves of HPLC peak areas of **1-D-Cleaved** and **1-Cleaved** that we constructed (Figures S25 and S26), we calculated the total cellular uptake of **1** by HEK 293 cells to be 13.15 fmol/cell. From the HPLC trace in Figure S24b (green trace) and the calibration curve of the HPLC peak areas of **2-D** that we constructed (Figure S27), we calculated the total cellular uptake of **2** by HEK 293 cells to be 11.20 fmol/cell.

^{19}F MR Imaging of GSH and Lgmn in Cells Treated with 1. The "on", "on", and "off" ^{19}F NMR signals, respectively, corresponding to **1**, **1** with HEK 293T cells, and **1** with

LI-1-treated HEK 293T cells, were also clearly imaged with ^{19}F MRI at 14.1 T. As shown in Figure 4, after 8×10^7 live HEK 293T cells were incubated with 2.5 mM **1** at 37 °C for 1 h, the ^{19}F MRI signals of the cells were "on", whereas the signals of the **LI-1**-pretreated cells incubated with **1** were "off". This result indicated that the "on" ^{19}F MRI signals from HEK 293T cells were induced by the GSH-controlled self-assembly and subsequent Lgmn-controlled disassembly of **1-NPs**. However, for HEK 293T cells incubated with **2**, the ^{19}F MRI signals were turned "off" due to the formation of **2-NPs**. The inhibition of Lgmn activity in HEK 293T cells by **LI-1** restored the ^{19}F MRI signal to the "on" state because the path for **2-NP** formation was blocked and **2** was only subjected to GSH reduction inside the cells.

^{19}F MR Imaging of Lgmn Tumors in Zebrafish with 1. **1** and **2** also were applied to ^{19}F MR imaging of Lgmn activity *in vivo* under a high magnetic field strength at 14.1 T. A zebrafish tumor model was chosen for this study for two reasons. First, the size of a 4 month old zebrafish is appropriate for a 5 mm (Φ) NMR tube for micro-MRI; second, the HEK 293T tumor model in a zebrafish was well-established and is easy to be verified.[33] Based on the methods previously reported,[33] the zebrafish were first given 25 Gy of gamma irradiation from a Cs-137 source (BIOBEAM2000, Eckert & Ziegler) at 1 Gy/min for 25 min. Two days later, 5 μL of a HEK 293T cell suspension (100 000 cells/μL) was injected into their enterocoelia. Two weeks later after cell injection, the HEK 293T tumors were clearly observed in the epigastria of the zebrafish, and the expression of Lgmn in the tumors was confirmed with immunofluorescence histology (Figure S28). Existence of HEK 293T tumors in the epigastria of the zebrafish was further verified by the strong red fluorescence emissions from DsRed (one type of red fluorescent proteins)-transfected HEK 293T tumors in the enterocoelia of irradiated casper zebrafish, while the unirradiated casper zebrafish only exhibited very weak fluorescence (Figure S29). About 5 μL of **1** (dissolved in dimethylsulfoxide, DMSO) was injected into the enterocoelia of a HEK 293T tumor-bearing zebrafish at a dose of 1.5 g/kg. Two hours after the injection, the zebrafish was imaged on a 14.1 T Bruker NMR/MRI system. We observed strong ^{19}F MRI signals from (or near) the tumors in zebrafish (topmost row in Figure 5). In contrast, healthy zebrafish, which had not received tumor implantation, did not show observable ^{19}F MRI signal after the injection of same dose of **1** (top middle row in Figure 5). These data indicated that the GSH-controlled, self-assembled **1-NPs** were cleaved and disassembled by Lgmn in HEK 293T tumors in zebrafish, turning on the ^{19}F MRI signals at (or near) the sites of the tumors. For **2** at the same dosage (*i.e.*, 1.5 g/kg), a very weak ^{19}F MRI signal was observed from the healthy zebrafish (Figure S30). Since **2** was only subjected to GSH reduction in healthy zebrafish (*i.e.*, no change of the transverse relaxation of the ^{19}F MR signal), 1.5 g/kg of **2** in healthy

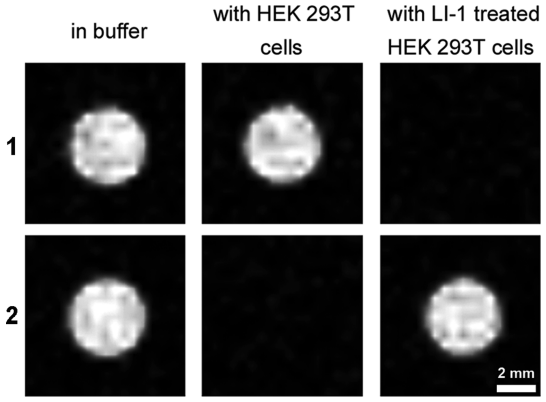

Figure 4. ^{19}F MR images of 1 (top) or 2 (bottom) at 2.5 mM in 500 μL of RIPA lysis buffer (left), in cell lysate after being incubated with HEK 293T cells at 37 °C for 1 h (middle), and in cell lysate after being incubated with LI-1-pretreated HEK 293T cells at 37 °C for 1 h (right). Scale bar: 2 mm.

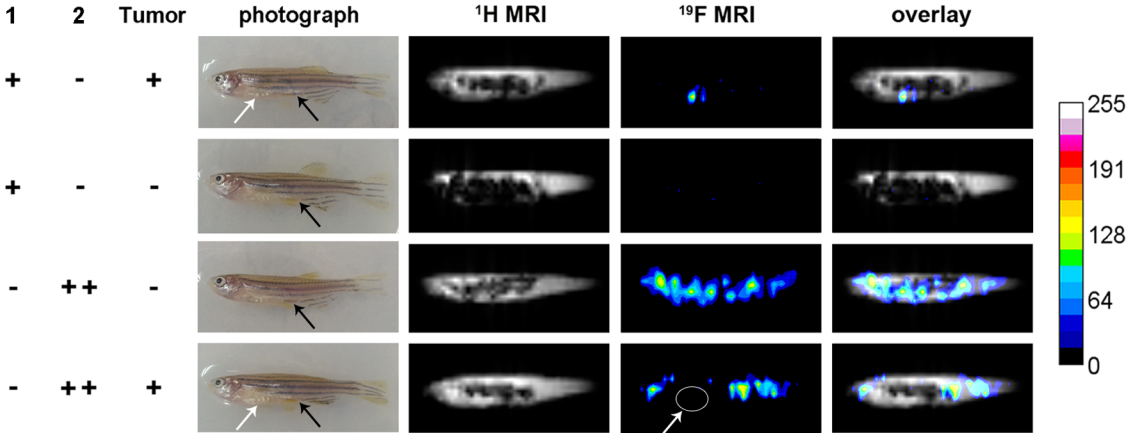

Figure 5. Topmost row: 1.5 g/kg of 1 (5 μL, dissolved in DMSO) was injected into the enterocoelia of HEK 293T tumor-bearing zebrafish. Top middle row, 1.5 g/kg of 1 (5 μL, dissolved in DMSO) was injected into the enterocoelia of a healthy zebrafish. Bottom middle row: 7.5 g/kg of 2 (5 μL, dissolved in DMSO) was injected into the enterocoelia of a healthy zebrafish. Bottommost row: 7.5 g/kg of 2 (5 μL, dissolved in DMSO) was injected into the enterocoelia of HEK 293T tumor-bearing zebrafish. White arrows indicate the tumor sites, and black arrows indicate the injection sites. White circle indicates the tumor location.

zebrafish did not result in "on" ^{19}F MRI signals similar to those of the 1.5 g/kg **1**-treated tumor-bearing zebrafish, implying that self-assembly and disassembly of **1-NPs** indeed could locally concentrate the ^{19}F probes and release them in the ROI. When the dose of **2** was increased to 7.5 g/kg, indiscriminate ^{19}F MRI signals could be observed from the healthy zebrafish without tumors (bottom middle row in Figure 5). Interestingly, when the HEK 293T tumor-bearing zebrafish were injected with **2** at 7.5 g/kg, discrete ^{19}F MRI signals from nontumor sites could be observed (bottom-most row in Figure 5). This result indicated that Lgmn in the HEK 293T tumors induced the self-assembly of **2-NPs** in tumors and thus turned the ^{19}F MRI signals "off".

CONCLUSIONS

In summary, by rational design of a biocompatible dual-functional fluorine probe **1**, we have developed a "smart" method of GSH-controlled assembly and Lgmn-controlled disassembly of **1-NPs** that turns the ^{19}F NMR signal "off" and then "on" for the sequential detection of GSH and Lgmn *in vitro* and in cells. With the ^{19}F NMR data obtained, we also successfully applied **1** for the ^{19}F MRI detection of Lgmn activities in zebrafish at low doses under 14.1 T. The *in vitro* and *in vivo* results suggest that this strategy of consecutive intracellular self-assembly and disassembly of ^{19}F NPs might be further applied to develop "smart" ^{19}F probes for clinical ^{19}F MRI diagnoses of diseases with low doses.

EXPERIMENTAL SECTION

^{19}F Nuclear Magnetic Resonance Methods. ^{19}F NMR experiments were performed on a Bruker Ascend WB 600 MHz spectrometer using a 4 mm broad-band N−C/F/H MAS probe. All ^{19}F NMR spectra were acquired with 3 s delays and accumulated 256 scans for a one-dimensional (1D) ^{19}F spectrum. The 1D ^{19}F spectrum was acquired with one pulse program with a 90 pulse width of 5.5 μs. ^{19}F chemical shifts were referenced to trifluoroacetic acid (TFA, −76.5 ppm). All the data were acquired and analyzed with Bruker's Topspin 3.1 software. All the experiments were performed at 25 °C.

^{1}H Magnetic Resonance Imaging Methods. ^{1}H magnetic resonance images of zebrafish in Figure 5 were obtained by flash method with a repetition time/echo time of 120/1.53 ms, a field of view of 6 × 6 cm without slice selection and accumulation, and a matrix size of 128 × 128. The excitation pulse width was 2740 Hz. The images were obtained at 25 °C.

^{19}F Magnetic Resonance Imaging. Images were acquired on a Bruker Ascend WB 600 MHz spectrometer using a Bruker Micro 5 imaging probe with triple axis gradients (maximum strength 200 G/cm) and an 8 mm diameter RF saddle coil. ^{19}F magnetic resonance images of phantom samples in Figure 4 were obtained by fast spin echo with a repetition time/echo time of 2000/7.9 ms using a flash imaging pulse sequence; the flip angle was 180°, field of view 3 × 3 cm, slice thickness 5 mm, matrix size 64 × 64, and the number of accumulations was 256. The excitation pulse width was 2740 Hz. All images were acquired and analyzed using Bruker's Para Vision 5.1 software. The original images were cropped and combined to create Figure 4.

^{19}F magnetic resonance images of zebrafish in Figure 5 were acquired by a flash method with repetition time/echo time of 100/3.56 ms; the flip angle was 30°, the field of view 6 × 6 cm, slice thickness 5 mm, matrix size 128 × 48, and the number of accumulations was 36 000. The excitation pulse width was 12 500 Hz. All the experiments were conducted at 25 °C.

Cell Experiment for ^{19}F NMR. For healthy HEK 293T cells, 4×10^6 live HEK 293T cells were trypsinized and collected into a 5 mL centrifuge tube. After the incubation of 500 μM **1** or **2** with HEK 293T cells in serum-free culture medium at 37 °C for 1 h, the cells were centrifuged (1000 rpm, 5 min) and washed three times with phosphate buffered saline (PBS) to remove the remaining probe. Then the cells were lysed with 100 μL of radioimmunoprecipitation assay (RIPA) lysis buffer for 30 min, and the supernatants were collected for ^{19}F NMR spectrometric analysis. For **LI-1**-treated HEK 293T cells, the HEK 293T cells were preincubated with 100 μM **LI-1** for 1 h. Then the cells were then treated with **1** or **2**, and the cell lysates were collected as described above.

Cell Experiment for ^{19}F MRI. For HEK 293T cells, 8×10^7 live HEK 293T cells were trypsinized and collected into a 5 mL centrifuge tube. After the incubation of 2.5 mM **1** or **2** with HEK 293T cells in serum-free culture medium at 37 °C for 1 h, the cells were centrifuged (1000 rpm, 5 min) and washed three times with PBS to remove the remaining probe. Then the cells were lysed with 500 μL of RIPA lysis buffer for 30 min, and the supernatants were collected for ^{19}F MRI spectrometric analysis. For **LI-1**-treated HEK 293T cells, the HEK 293T cells were preincubated with 100 μM **LI-1** for 1 h. Then the cells were treated with **1** or **2**, and the cell lysates were collected as described above.

Immunohistochemistry. Adult zebrafish was fixed in 4% freshly made paraformaldehyde. Then the whole fish was sliced at 8 μm intervals with Leica CM 1950 (Germany) cryosection machine. After being washed for 5 min with PBS three times, the slices were blocked with 10% PBST, and a first antibody was added for overnight at 4 °C. Next, the slices were washed wish PBS three times, and a second antibody was applied for 2 h at room temperature. After being washed with PBS and mounted in 80% glycerol, the slices were imaged with an Olympus BX61 confocal microscope (Japan).

Conflict of Interest: The authors declare no competing financial interest.

Supporting Information Available: Experimental methods and details; characterization details; HPLC conditions; Schemes S1 and S2; Figures S1−S30; and Tables S1−S7. This material is available free of charge *via* the Internet at http://pubs.acs.org.

Acknowledgment. This work was supported by Collaborative Innovation Center of Suzhou Nano Science and Technology, the Major Program of Development Foundation of Hefei Center for Physical Science and Technology, the National Natural Science Foundation of China (Grants 21375121, 91127036, 21175122, and 21372222).

REFERENCES AND NOTES

1. Liu, C.; Sun, C.; Huang, H.; Janda, K.; Edgington, T. Overexpression of Legumain in Tumors Is Significant for Invasion/Metastasis and a Candidate Enzymatic Target for Prodrug Therapy. *Cancer Res.* **2003**, *63*, 2957–2964.
2. Manoury, B.; Hewitt, E. W.; Morrice, N.; Dando, P. M.; Barrett, A. J.; Watts, C. An Asparaginyl Endopeptidase Processes a Microbial Antigen for Class II MHC Presentation. *Nature* **1998**, *396*, 695–699.
3. Miller, G.; Matthews, S. P.; Reinheckel, T.; Fleming, S.; Watts, C. Asparagine Endopeptidase Is Required for Normal Kidney Physiology and Homeostasis. *FASEB J.* **2011**, *25*, 1606–1617.
4. Edgington, L. E.; Verdoes, M.; Ortega, A.; Withana, N. P.; Lee, J.; Syed, S.; Bachmann, M. H.; Blum, G.; Bogyo, M. Functional Imaging of Legumain in Cancer Using a New

Quenched Activity-Based Probe. *J. Am. Chem. Soc.* **2012**, *135*, 174–182.
5. Watts, C. The Exogenous Pathway for Antigen Presentation on Major Histocompatibility Complex Class II and CD1Molecules. *Nat. Immunol.* **2004**, *5*, 685–692.
6. Choi, S. J.; Reddy, S. V.; Devlin, R. D.; Menaa, C.; Chung, H.; Boyce, B. F.; Roodman, G. D. Identification of Human Asparaginyl Endopeptidase (Legumain) as an Inhibitor of Osteoclast Formation and Bone Resorption. *J. Biol. Chem.* **1999**, *274*, 27747–27753.
7. Liu, Y.; Bajjuri, K. M.; Liu, C.; Sinha, S. C. Targeting Cell Surface Alpha(v)beta(3) Integrin Increases Therapeutic Efficacies of a Legumain Protease-Activated Auristatin Prodrug. *Mol. Pharmaceutics* **2012**, *9*, 168–175.
8. Hanahan, D.; Weinberg, R. A. Hallmarks of Cancer: The Next Generation. *Cell* **2011**, *144*, 646–674.
9. Cheng, K.; Yang, M.; Zhang, R.; Qin, C.; Su, X.; Cheng, Z. Hybrid Nanotrimers for Dual T_1 and T_2-Weighted Magnetic Resonance Imaging. *ACS Nano* **2014**, *8*, 9884–9896.
10. Chakravarty, R.; Valdovinos, H. F.; Chen, F.; Lewis, C. M.; Ellison, P. A.; Luo, H.; Meyerand, M. E.; Nickles, R. J.; Cai, W. Intrinsically Germanium-69-Labeled Iron Oxide Nanoparticles: Synthesis and *In-Vivo* Dual-Modality PET/MR Imaging. *Adv. Mater.* **2014**, *26*, 5119–5123.
11. Farr, T. D.; Lai, C. H.; Grünstein, D.; Orts-Gil, G.; Wang, C. C.; Boehm-Sturm, P.; Seeberger, P. H.; Harms, C. Imaging Early Endothelial Inflammation Following Stroke by Core Shell Silica Superparamagnetic Glyconanoparticles That Target Selectin. *Nano Lett.* **2014**, *14*, 2130–2134.
12. MacDonald, T. D.; Liu, T. W.; Zheng, G. An MRI-Sensitive, Non-photobleachable Porphysome Photothermal Agent. *Angew. Chem., Int. Ed.* **2014**, *53*, 6956–6959.
13. Klippel, S.; Freund, C.; Schröder, L. Multichannel MRI Labeling of Mammalian Cells by Switchable Nanocarriers for Hyperpolarized Xenon. *Nano Lett.* **2014**, *14*, 5721–5726.
14. Mizukami, S.; Takikawa, R.; Sugihara, F.; Hori, Y.; Tochio, H.; Wälchli, M.; Shirakawa, M.; Kikuchi, K. Paramagnetic Relaxation-Based ^{19}F MRI Probe To Detect Protease Activity. *J. Am. Chem. Soc.* **2008**, *130*, 794–795.
15. Code, R. F.; Harrison, J. E.; McNeill, K. G.; Szyjkowski, M. *In Vivo* ^{19}F Spin Relaxation in Index Finger Bones. *Magn. Reson. Med.* **1990**, *13*, 358–369.
16. Danielson, M. A.; Falke, J. J. Use of ^{19}F NMR To Probe Protein Structure and Conformational Changes. *Annu. Rev. Biophys. Biomol. Struct.* **1996**, *25*, 163–195.
17. Cui, W.; Otten, P.; Li, Y.; Koeneman, K. S.; Yu, J.; Mason, R. P. Novel NMR Approach To Assessing Gene Transfection: 4-Fluoro-2-nitrophenyl-β-D-galactopyranoside as a Prototype Reporter Molecule for β-Galactosidase. *Magn. Reson. Med.* **2004**, *51*, 616–620.
18. Takaoka, Y.; Sakamoto, T.; Tsukiji, S.; Narazaki, M.; Matsuda, T.; Tochio, H.; Shirakawa, M.; Hamachi, I. Self-Assembling Nanoprobes That Display Off/On ^{19}F Nuclear Magnetic Resonance Signals for Protein Detection and Imaging. *Nat. Chem.* **2009**, *1*, 557–561.
19. Higuchi, M.; Iwata, N.; Matsuba, Y.; Sato, K.; Sasamoto, K.; Saido, T. C. ^{19}F and ^{1}H MRI Detection of Amyloid Beta Plaques *in Vivo*. *Nat. Neurosci.* **2005**, *8*, 527–533.
20. Takaoka, Y.; Kiminami, K.; Mizusawa, K.; Matsuo, K.; Narazaki, M.; Matsuda, T.; Hamachi, I. Systematic Study of Protein Detection Mechanism of Self-Assembling ^{19}F NMR/MRI Nanoprobes toward Rational Design and Improved Sensitivity. *J. Am. Chem. Soc.* **2011**, *133*, 11725–11731.
21. Tanaka, K.; Kitamura, N.; Naka, K.; Chujo, Y. Multi-modal ^{19}F NMR Probe Using Perfluorinated Cubic Silsesquioxane-Coated Silica Nanoparticles for Monitoring Enzymatic Activity. *Chem. Commun.* **2008**, *46*, 6176–6178.
22. Tanaka, K.; Kitamura, N.; Chujo, Y. Bimodal Quantitative Monitoring for Enzymatic Activity with Simultaneous Signal Increases in ^{19}F NMR and Fluorescence Using Silica Nanoparticle-Based Molecular Probes. *Bioconjugate Chem.* **2011**, *22*, 1484–1490.
23. Tanabe, K.; Harada, H.; Narazaki, M.; Tanaka, K.; Inafuku, K.; Komatsu, H.; Ito, T.; Yamada, H.; Chujo, Y.; Matsuda, T.; et al. Monitoring of Biological One-Electron Reduction by ^{19}F NMR Using Hypoxia Selective Activation of an ^{19}F-Labeled Indolequinone Derivative. *J. Am. Chem. Soc.* **2009**, *131*, 15982–15983.
24. Oishi, M.; Sumitani, S.; Nagasaki, Y. On-Off Regulation of ^{19}F Magnetic Resonance Signals Based on pH-Sensitive PEGylated Nanogels for Potential Tumor-Specific Smart ^{19}F MRI Probes. *Bioconjugate Chem.* **2007**, *18*, 1379–1382.
25. Kenwright, A. M.; Kuprov, I.; De Luca, E.; Parker, D.; Pandya, S. U.; Senanayake, P. K.; Smith, D. G. ^{19}F NMR Based pH Probes: Lanthanide(III) Complexes with pH-Sensitive Chemical Shifts. *Chem. Commun.* **2008**, 2514–2516.
26. Yuan, Y.; Sun, H.; Ge, S.; Wang, M.; Zhao, H.; Wang, L.; An, L.; Zhang, J.; Zhang, H.; Hu, B.; et al. Controlled Intracellular Self-Assembly and Disassembly of ^{19}F Nanoparticles for MR Imaging of Caspase 3/7 in Zebrafish. *ACS Nano* **2015**, *9*, 761–768.
27. Liang, G.; Ren, H.; Rao, J. A Biocompatible Condensation Reaction for Controlled Assembly of Nanostructures in Living Cells. *Nat. Chem.* **2010**, *2*, 54–60.
28. Ren, H.; Xiao, F.; Zhan, K.; Kim, Y.; Xie, H.; Xia, Z.; Rao, J. A Biocompatible Condensation Reaction for the Labeling of Terminal Cysteine Residues on Proteins. *Angew. Chem., Int. Ed.* **2009**, *48*, 9658–9662.
29. Lee, J.; Bogyo, M. Development of Near-Infrared Fluorophore (NIRF)-Labeled Activity-Based Probes for *In Vivo* Imaging of Legumain. *ACS Chem. Biol.* **2010**, *5*, 233–243.
30. Rendón-Gandarilla, F. J.; Ramón-Luing, L. A.; Ortega-López, J.; Rosa de Andrade, I.; Benchimol, M.; Arroyo, R. The TvLEGU-1, a Legumain-like Cysteine Proteinase, Plays a Key Role in *Trichomonas vaginalis* Cytoadherence. *Cancer Res.* **2013**, *2013*, 18.
31. Dopp, E.; von Recklinghausen, U.; Hartmann, L. M.; Stueckradt, I.; Pollok, I.; Rabieh, S.; Hao, L.; Nussler, A.; Katier, C.; Hirner, A. V.; et al. Subcellular Distribution of Inorganic and Methylated Arsenic Compounds in Human Urothelial Cells and Human Hepatocytes. *Drug Metab. Dispos.* **2008**, *36*, 971–979.
32. Gao, Y.; Shi, J.; Yuan, D.; Xu, B. Imaging Enzyme-Triggered Self-Assembly of Small Molecules Inside Live Cells. *Nat. Commun.* **2012**, *3*, 1033.
33. White, R. M.; Sessa, A.; Burke, C.; Bowman, T.; LeBlanc, J.; Ceol, C.; Bourque, C.; Dovey, M.; Goessling, W.; Burns, C. E.; et al. Transparent Adult Zebrafish as a Tool for *In Vivo* Transplantation Analysis. *Cell Stem Cell* **2008**, *2*, 183–189.